

# Meditating Metal Coenhanced Fluorescence and SERS Around Gold Nanoaggregates in Nanosphere as Bifunctional Biosensor for Multiple DNA Targets

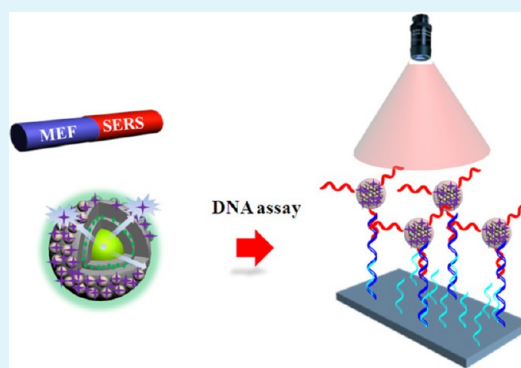
Yong Liu and Peiyi Wu\*

State Key Laboratory of Molecular Engineering of Polymers, Department of Macromolecular Science, and Laboratory of Advanced Materials, Fudan University, Shanghai 200433, People's Republic of China

**S** Supporting Information

**ABSTRACT:** Gold nanoparticles (Au NPs) are very attractive candidate nanoparticles in biological assay because of their high chemical stabilities, high homogeneities, good biocompatibilities, and low toxicities. However, molecular beacon assays via encapsulating the combined fluorescence or surface-enhanced Raman scattering (SERS) signals of reporters and Au NPs in nanobarcodes particles usually suffer from fluorescence quenching or weak Raman enhancement when Au NPs are employed (especially with size smaller than 15 nm). Herein, we present a new design of simultaneously realizing metal-enhanced fluorescence and coenhanced surface-enhanced Raman scattering by facilely embedding Ag nanoparticle into the shell of two kinds of Au nanoaggregate (5 and 10 nm), meanwhile, fluorophore is located between the silver core and gold nanoparticle layers and the distance among them is adjusted by SiO<sub>2</sub> spacer (Ag@first SiO<sub>2</sub> spacer@FITC+SiO<sub>2</sub>@second SiO<sub>2</sub> spacer@Au nanoaggregate). In this architecture, Ag nanoparticle not only is utilized as an efficient fluorescence enhancer to overcome the common fluorescence quenching around Au nanoaggregates but also behaves like a mirror. Thus, incident light that passes through the SERS-active Au nanoaggregate and the intervening dielectric layer of SiO<sub>2</sub> could be reflected multiply from the surface of Ag nanoparticle and coupled with the light at the nanogap between the Au nanoaggregates to further amplify Raman intensity. This results in enhancement factors for fluorescence and SERS ~1.6-fold and more than 300-fold higher than the control samples without silver core under identical experimental conditions, respectively. Moreover, fluorophore and SERS reporters are assembled onto different layers of the concentric hybrid microsphere, resulting in a feasible fabrication protocol when a large number of agents need to be involved into the dual-mode nanobarcodes. A proof-of-concept chip-based DNA sandwich hybridization assay using genetically modified organisms as a model system has been investigated based on the concentric hybrid microsphere. The high specificity and sensitivity of the assays suggest that the new architecture has a potential for various bioanalytical applications and provides opportunities for other similar metal nanoparticles to realize coenhancement effect.

**KEYWORDS:** metal-enhanced fluorescence, SERS, genetically modified organisms, DNA sandwich hybridization



## INTRODUCTION

Plasmonic nanostructures have attracted the increasing attention of researchers for widespread use in solar cells,<sup>1,2</sup> photocatalyst,<sup>3</sup> optical spectroscopy-based immunoassays,<sup>4</sup> and data storage.<sup>5</sup> The electric fields of plasmonic nanostructures are greatly enhanced when the localized surface plasmon is in resonance with the incident light, and concomitantly augment the interaction of light with molecules in the proximity of the surface, giving rise to phenomena such as metal-enhanced fluorescence (MEF) and surface-enhanced Raman scattering (SERS). In the last decades, with the integration of increased brightness, photostability, reduced blinking for MEF and high sensitivity, noninvasive sampling, and insensitivity to water for SERS, they have been subjected to extensive application in the rapid and sensitive identification and detection of chemical and biological species,<sup>6</sup> molecular imaging,<sup>7</sup> and disease monitoring

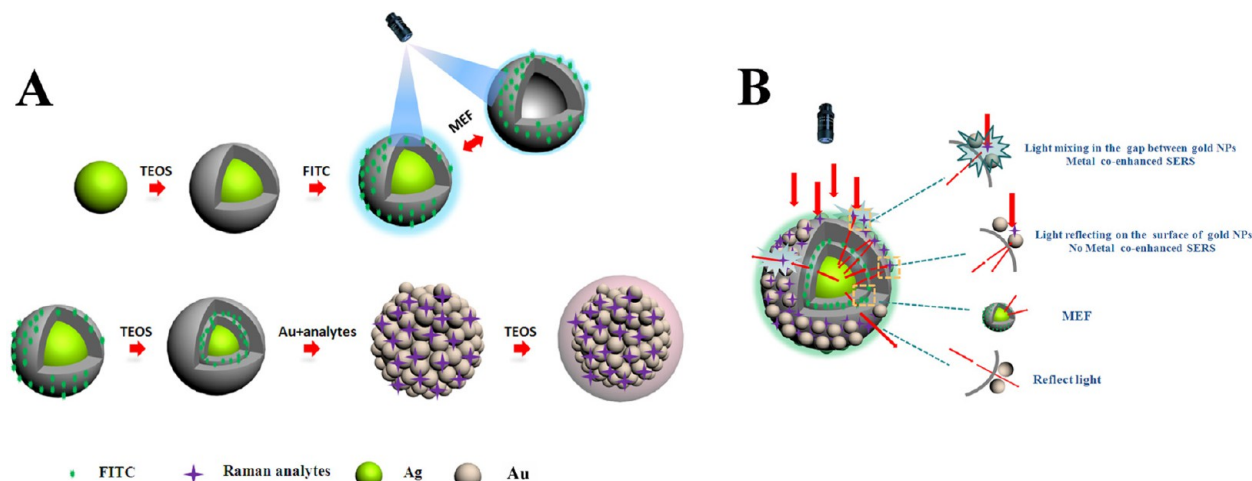
at cellular,<sup>8,9</sup> tissue, and animal levels.<sup>10</sup> The plasmonic nanostructures that have been typically utilized for fluorescence and Raman enhancement are based on silver and gold on account of their strong enhancement in the visible and near-infrared region.<sup>11</sup> Although single colloidal nanoparticle-based MEF and SERS assays have shown promising application in various fields, they are still limited by the poor sensitivity due to the low electromagnetic field around the metallic surface. Nanoparticle aggregates will make the largest contribution to MEF and SERS because of the electromagnetic field that is concentrated at the nanogaps or clefts (hot spots) of the aggregate, promoting the signal of fluorescence and especially

**Received:** April 21, 2013

**Accepted:** June 4, 2013

**Published:** June 4, 2013

Scheme 1. (A) Strategy for the Synthesis of SERS-MEF Nanobarcode and (B) the Incident and Reflective Coenhanced SERS



SERS by many orders of magnitude. In line with this, a number of nanofabrication techniques (e.g., wet chemical reduction,<sup>12</sup> electromigration,<sup>13</sup> lithography,<sup>14</sup> vapor deposition<sup>15</sup>) have been developed toward fabricating metallic substrates in different configurations, such as silver and gold nanoaggregate,<sup>16</sup> Au–Ag nanocomposite substrates,<sup>17</sup> dimers,<sup>18</sup> trimers,<sup>19</sup> regular arrays<sup>20,21</sup> for maximize SERS and MEF, and in some cases, single molecule detection could be realized.<sup>22</sup>

Despite the tremendous enhancement at the hotspots, it is conceivable that if an appropriate optical element is coupled with the plasmonic structure of aggregated metal nanoparticles, it could further improve the electric field at the hotspots and induce plasmon effect without the need for rigorous tuning the distance of nanogap or fabricating novel nanostructures with complicated and expensive technology. Afterward, metal-enhanced fluorescence and an additional enhancement of SERS could be achieved. Tao et al.<sup>23</sup> employed a new strategy to efficiently enhance fluorescence on the basis of coupling surface plasmons of metal particles with optical properties of colloidal photonic crystals. Akselrod et al.<sup>24</sup> reported a 20-fold enhancement in the fluorescence of the organic dye DCM on a critically coupled resonator, which absorbed nearly all of the incident light because of the destructive interference between light reflected by the mirror and light reflected by the J-aggregate. Silver nanoparticle/4-mercaptopyridine (4-Mpy)/silver film sandwich substrate based on evanescent field and Au nanoparticle (NP)-overmirror (NPOM) configuration with varying but thin atomic layer-deposited oxide spacer were fabricated for localized and propagating surface plasmon coenhanced Raman spectroscopy.<sup>25,26</sup> More recently, to probe the structural characteristics and properties of the newly arisen graphene as the thinnest material in nature, researchers proposed a specifically designed substrate of Si capped with surface-active metal (Ag) and oxide double layers (SMO) as a novel surface and interference coenhanced Raman scattering technique to dramatically enhance the Raman signal intensity of graphene.<sup>27</sup>

Inspired by the planar interference and surface coenhanced fluorescence or Raman scattering, in this study, core–shell structures, representing multiple-discrete functions related components integrated in one unit, were fabricated to simultaneously realize metal enhanced fluorescence and interference and surface coenhanced Raman scattering through

facilely embedding Ag NPs instead of highly reflective Ag, Al, or Si mirror into Au NPs aggregates shell, between which the distance is adjusted by a dielectric spacer layer of silica with varying thickness. Meanwhile, fluorophores are buried between the Ag NPs and Au aggregates. The detailed fabrication process is illustrated in Scheme 1. The motivation for this work is 3-fold. First, gold NPs are employed as an typical outer SERS-active substrate in our study because of their usually weaker Raman enhancement effect compared with Ag NPs and they are the kind of “super quencher”, quenching the fluorescence of a range of dyes primarily arising from nonradiative energy transfer from the dye to the metal in spite of its stability, biocompatibility, and lack of toxicity. Second, Ag nanoparticles of sufficient size in favorable media can reach a scattering fraction well over 90%, similar to an Ag mirror with 97% reflectivity.<sup>28</sup> The plasmonic properties of the SERS substrate could be manipulated by choosing an appropriate dielectric thickness to favor the multiple reflections of the incident laser at the upper and lower surfaces of the dielectric layer to induce the interference phenomenon at the hot spots of Au aggregate, bringing about the interference and surface coenhanced Raman scattering. Third, the localized surface plasmon by Ag NPs could also induce stronger MEF when fluorophores are separated from their surface, then apart from an increase in the fluorophore brightness, the number of excitation cycles that a molecule can survive before photobleaching will be improved because of the reduced excited-state lifetimes. In our study, the enhancement factors for fluorescence and SERS can reach  $\sim 1.6$  and more than the order of  $1 \times 10^2$  times compared with that without Ag core, respectively. We anticipate that this core shell microsphere, designated as MEF-SERS, could be more suitable for biophysical studies or biosensor applications than planar solid substrates. As a proof-in-principle experiment, dual-mode nanotags based on the MEF-SERS NPs for DNA detection were demonstrated using multiplex sandwich immunoassays. The distinct and strong optical signals of probe-conjugated MEF-SERS nanobarcode afford target DNA detection more sensitivity and accuracy.

## EXPERIMENTAL SECTION

**Materials.** All chemicals were of analytical grade and used without further purification.  $\text{AgNO}_3$ , ethylene glycol, Hydrochloroauric acid, NaCl, acetone, tetraethyl orthosilicate (TEOS), 3-glycidyloxypropyltrimethoxysilane (GMPTS), 3-aminopropyltrimethoxysilane

(APTMS) (97%), and ammonia aqueous solution (28 wt %) were purchased from Sinopharm Chemical Reagent Co. (China). Polyvinylpyrrolidone (PVP,  $M_w = 55\,000$ ), Fluorescein isothiocyanate (FITC) were obtained from Sigma Aldrich. 1-Ethyl-3-(3-dimethylaminopropyl) carbodiimide hydrochloride (EDC), *N*-hydroxysulfosuccinimide (Sulfo-NHS), succinic anhydride, *N,N*-dimethylformamide, toluene, sodium borohydride, anhydrous ethanol, Raman reporter molecules, including 4-methylbenzenethiol (4-MT), 2-fluorobenzenethiol (2-FBT), 4-chlorobenzenethiol (4-CBT), 2-naphthalenethiol (2-NT) were purchased from Aladdin Reagent Co., Ltd. (Shanghai, China). Nucleotide sequences of target GMOs and the corresponding probes and captures were purchased from Sangon Biotech (Shanghai) Co., Ltd. and purified using high-performance liquid chromatography. Probe DNAs and capture DNAs were modified with amine groups at the 5' and 3' end, respectively. Deionized water was used in all experiments.

**Synthesis of Ag@first SiO<sub>2</sub> Spacer Microspheres.** Ag nanoparticles with diameter about 55 nm were synthesized by a modified method reported by Zhao et al.<sup>29</sup> The Ag@SiO<sub>2</sub> microspheres with different silica thickness were synthesized through a versatile Stöber sol–gel method as follows.

**Ag@SiO<sub>2</sub>-3 nm, Ag@SiO<sub>2</sub>-8 nm.** Ag nanoparticle obtained above (100 mg) was added to a three-neck round-bottom flask charged with a mixture of ethanol (80 mL), water (20 mL) and ammonia aqueous solution (1 mL, 28 wt %) under ultrasound for 15 min. Afterward, 18  $\mu$ L of TEOS in 2 mL of ethanol solution was added dropwise with continuous stirring in 2 min and the reaction was allowed to proceed for 8 h at 27 °C. The Ag@SiO<sub>2</sub> microsphere was separated by centrifugation and washed by ethanol and water for several times. Silica layer thickness of about 8 nm (Ag@SiO<sub>2</sub>-8 nm) was obtained using a procedure similar to the above by increasing TEOS concentration to 60  $\mu$ L.

**Ag@SiO<sub>2</sub>-18 nm, Ag@SiO<sub>2</sub>-36 nm.** To a flask was added the Ag nanoparticle obtained above (100 mg) to a mixture of ethanol (280 mL), water (70 mL) and ammonia aqueous solution (3.5 mL, 28 wt %) under stirring for 15 min, followed by addition of 4 mL of TEOS in four portions over a time interval of 30 min. After completion of TEOS addition, the mixture was allowed to react for 10 h before the nanoparticles were harvested by centrifugation at 12000 rpm for 5 min. The precipitate was washed with copious amounts of water and ethanol respectively and finally redispersed in 20 mL of ethanol. Ag@SiO<sub>2</sub>-36 nm was obtained by utilizing Ag@SiO<sub>2</sub>-18 nm NPs as the seeding materials with a second coating cycle.

**Preparation of Ag@first SiO<sub>2</sub> Spacer@SiO<sub>2</sub>-FITC Microspheres.** First, to a clean and dry test tube were added 8 mg (21  $\mu$ mol) of FITC, 15  $\mu$ L (64  $\mu$ mol) of APTMS and 5 mL of EtOH, followed by gently stirring in darkness in a N<sub>2</sub> atmosphere for 24 h to allow the coupling reaction between the amine and isothiocyanate groups and form APTMS-FITC. Next, 0.1 g of Ag@SiO<sub>2</sub> particles with different shell thickness was dissolved in a mixture of ethanol (80 mL), water (20 mL), and ammonia aqueous solution (1 mL, 28 wt %) under stirring, 70  $\mu$ L of APTMS-FITC was then added slowly. The reaction was continued for 15 min followed by adding 36  $\mu$ L TEOS to the mixture. And then the reaction was continued for 8 h. The Ag@first SiO<sub>2</sub> spacer@SiO<sub>2</sub>-FITC microspheres were separated by centrifugation and washed by ethanol and water for four times, the thickness of SiO<sub>2</sub>-FITC layer was about 3 nm. The Ag@first SiO<sub>2</sub> spacer@SiO<sub>2</sub>-FITC microspheres were denominated according to the silica spacing layer thickness as MEF-1 (SiO<sub>2</sub> thickness = 3 nm), MEF-2 (SiO<sub>2</sub> thickness = 8 nm), MEF-3 (SiO<sub>2</sub> thickness = 18 nm), and MEF-4 (SiO<sub>2</sub> thickness = 36 nm), respectively. The control sample was obtained by etching Ag core of Ag@first SiO<sub>2</sub> spacer@SiO<sub>2</sub>-FITC microspheres and then formed hollow silica nanoshells. The detailed experiment process is shown in the Supporting Information.

**Preparation of Ag@SiO<sub>2</sub>-8 nm@FITC+SiO<sub>2</sub>@second SiO<sub>2</sub> Spacer Microspheres (MEF-2@ second SiO<sub>2</sub> spacer).** MEF-2 was chosen in virtue of its maximum fluorescence enhancement efficiency discussed in the following text. MEF-2@second SiO<sub>2</sub> spacer microspheres with different thickness of the second SiO<sub>2</sub> layers were

prepared similarly to the above-mentioned SiO<sub>2</sub> encapsulation method.

**MEF-2@SiO<sub>2</sub>-8 nm, MEF-2@SiO<sub>2</sub>-18 nm, MEF-2@ SiO<sub>2</sub>-36 nm Microspheres.** The MEF-2@second SiO<sub>2</sub> spacer particles with 8, 18, and 36 nm thickness of the second silica layer could be easily obtained by replacing the Ag or Ag-SiO<sub>2</sub> in the synthesis of Ag@SiO<sub>2</sub>-8 nm, Ag@SiO<sub>2</sub>-18 nm, and Ag@SiO<sub>2</sub>-36 nm with MEF-2 individually.

**MEF-2@SiO<sub>2</sub>-26 Microspheres.** In brief, the obtained 0.1 g of MEF-2@SiO<sub>2</sub>-18 nm microspheres were dissolved in the mixture of ethanol (80 mL) and water (20 mL) and 1 mL of ammonia aqueous solution (28 wt %) with stirring, then 60  $\mu$ L of TEOS was added followed by stirring gently for 8 h. The MEF-2@ SiO<sub>2</sub>-26 nm microspheres were separated by centrifugation and washed by ethanol and water for several times.

**Synthesis of Ag@SiO<sub>2</sub>-8 nm@FITC+SiO<sub>2</sub>@second SiO<sub>2</sub> Spacer @Au Microspheres (MEF-2@second SiO<sub>2</sub> spacer@Au).** **MEF-2@second SiO<sub>2</sub> Spacer@5 nm-Au Seed.** The MEF-2@sceond SiO<sub>2</sub> spacer@5 nm-Au seed microspheres were synthesized by the deposition-precipitation (DP) method.<sup>30</sup> First, 300  $\mu$ L of APTMS was added to MEF-2@sceond SiO<sub>2</sub> spacer NPs ethanol solution (10 mL, 1 mg/mL) followed by refluxed for 6 h at 85 °C, then the APTMS modified MEF-2@sceond SiO<sub>2</sub> spacer NPs were obtained by centrifugation and washed by ethanol and water for four times. Second, 2.25 mL of 0.1 M NaOH was added to 10 mL of a 6.35 mM HAuCl<sub>4</sub> solution, and then 10 mg of APTMS modified MEF-2@sceond SiO<sub>2</sub> spacer NPs were dispersed with vigorous stirring and warmed to 96 °C for 30 min. The MEF-2@sceond SiO<sub>2</sub> spacer@5 nm-Au were collected using a centrifuge and washed with copious amounts of water and ethanol, respectively.

**MEF-2@second SiO<sub>2</sub> Spacer@10 nm-Au.** Potassium–gold solutions (K-gold) were prepared by mixing 200 mL aqueous K<sub>2</sub>CO<sub>3</sub> solutions (280 mg solid/L) with 3.8 mL of 25 mM HAuCl<sub>4</sub> stock solution by continuous stirring and aging in the dark for 12 h. Then the above MEF-2@sceond SiO<sub>2</sub> spacer@5 nm-Au seed was added to 28 mL of K-gold solution and 1.3 mL of 0.0053 M NaBH<sub>4</sub> was subsequently added quickly, the reaction was continued for 10 min and then collected using a centrifuge and washed with copious amounts of water and ethanol, respectively.

**Preparation of Ag@8 nm-SiO<sub>2</sub>@FITC+SiO<sub>2</sub>@SiO<sub>2</sub>-26 nm@Au +reporter@SiO<sub>2</sub> Microspheres (MEF-2@SiO<sub>2</sub>-26 nm@10 nm-Au +reporter@SiO<sub>2</sub>) as MEF-SERS Nanobarcode NPs.** MEF-2@SiO<sub>2</sub>-26 nm@10 nm-Au was chosen due to its stability discussed in the following text. Ten milligrams of MEF-2@SiO<sub>2</sub>-26 nm@10 nm-Au microspheres were dispersed in a mixture of 10 mL of 1 wt % APTES ethanol solution and 10 mL of 1 mM Raman reporter ethanol solution by sonication and kept quiescent for 12 h at 4 °C. The resulting product was harvested by centrifugation and washed with copious amounts of anhydrous ethanol to remove excess APTES and Raman reporters, and then the products were dispersed in a mixture of 10 mL of water, 38 mL of ethanol, and 1 mL of ammonia solution by sonication for 10 min. Then 0.05 g of TEOS in 2 mL ethanol was added followed by sonication for another 60 min at 0 °C. The resultant multilayer core–shell MEF-2@SiO<sub>2</sub>-26 nm@Au+reporter@SiO<sub>2</sub> microspheres were collected by centrifugation and washed with water and ethanol for 4 times, respectively. It appeared that every specific type of Raman reporter could be clearly identified based on their unique spectroscopic fingerprints, and the outmost SiO<sub>2</sub> layer will prevent the interference from other Raman reporters. Moreover, the characteristic SERS bands for each tag were clearly distinguishable as labeled with objects. Thereby, it could behave like nanobarcodes and detect various biomolecules simultaneously when labeled with these different tags or their multiplex combination, thus abbreviated as MEF-SERS nanobarcodes.

**Conjugation of MEF-SERS Nanobarcodes with Probe DNA Strands (probe DNA-functionalized MEF-SERS nanobarcodes).** First, 300  $\mu$ L of APTMS was added to MEF-SERS nanobarcodes (10 mL, 1 mg/mL) followed by being refluxed for 6 h at 85 °C, and then the APTMS modified MEF-SERS nanobarcodes were obtained by centrifugation and washed by ethanol and water four times. Next, 10.0 mg of the APTMS-modified MEF-SERS nanobarcodes was added in



the DMF solution of succinic anhydride (20 mL, 10 wt %). The mixture was stirred for 24 h at room temperature. After that, the product was collected by centrifugation, washed with ethanol, and dried under a vacuum. The synthesized sample was denoted as MEF-SERS-COOH. Third, 2.5 mg of EDC and 1.2 mg of Sulfo-NHS were added to the 2 mL of phosphate buffer (PB, pH 7.4) containing 2 mg of MEF-SERS-COOH microspheres to activate the COOH group. After incubation for 30 min, 400  $\mu$ L of 1  $\mu$ M probe DNA was added and vortex-mixed overnight. The solution was centrifuged and washed by PBS solution to obtain the probe DNA-functionalized MEF-SERS nanobarcodes, which were dispersed in 10 mL of PBS solution for future use.

**Immobilization of Capture DNA on a Glass Substrate (capture-DNA-modified chip).** A glass substrate (chip, 1 cm  $\times$  1 cm  $\times$  0.1 cm) was first immersed in piranha solution (30 wt % hydrogen peroxide and 70 wt % sulfuric acid) for 12 h, and then washed thoroughly with water and dried under vacuum. The obtained substrate was silylanized by adding it to 10 mL of toluene solution containing 300  $\mu$ L of GPTMS and was refluxed at 120  $^{\circ}$ C for 6 h. Afterward, the epoxylated substrate was washed completely with ethanol and water to remove physically adsorbed GPTMS and dried under a stream of nitrogen. Ten microliters of capture DNA strands (1  $\mu$ M) in 10 mM PBS (pH 7.4) was dropped on the epoxylated substrate and reacted at room temperature for 5 h. After the substrate was washed three times with 10 mM PBS (pH 7.4) and the remaining active epoxy groups were reduced with sodium borohydride (2 mg in a mixture of 6 mL of PBS at a pH of 7.4 and 2 mL ethanol). The as-prepared capture DNA-modified chip was then rinsed with water and stored at 4  $^{\circ}$ C until use.

**Multiplex DNA Sequence Detection of Genetically Modified Organisms Using MEF-SERS Nanobarcodes.** First, The hybridization reaction was carried out by dropping 10  $\mu$ L of target DNA solution (1  $\mu$ M) prepared with 0.6 M NaCl 10 mM PBS (pH 7.4) on the capture-DNA-modified chip and incubating them at room temperature for 5 h. After being washed with 10 mM PBS (pH 7.4) three times, the chip was immersed in the above obtained aqueous dispersion of probe-DNA-functionalized MEF-SERS nanobarcodes in 0.6 M NaCl 10 mM PBS (pH 7.4) and incubated at room temperature for 5 h. Afterward, the chip was washed with 10 mM PBS (pH 7.4) several times and sonicated for 30 s to remove physically adsorbed SERS probes. The resultant sandwich-type hybridization chip was dried under a stream of nitrogen for SERS and fluorescence measurement.

**Characterization Methods.** The transmission electron microscope (TEM) images were taken with a JEOL JEM-2100F microscope (Japan) equipped with electron diffraction. Field-emission scanning electron microscopy (FE-SEM) was performed on a Hitachi S-4800 electron microscope. The elemental contents were measured using inductively coupled plasma-atomic emission spectrometry (ICP-AES, Varian VISTA-MPX). Hydrodynamic diameter measurements were conducted by dynamic light scattering (DLS) with a ZEN3600 (Malvern, UK) Nano ZS instrument using He–Ne laser at a wavelength of 632.8 nm. Wide-angle XRD patterns were recorded on a Bruker D8 diffractometer (Germany) with Ni-filtered Cu  $K\alpha$  radiation. Ultraviolet–visible (UV–vis) absorption spectra were measured on a UV-3150 spectrometer (Shimadzu, Japan). Raman spectra were collected on a Renishaw Via Reflex micro-Raman spectrometer with 514 and 633 nm laser excitation. The data acquisition time was usually 10 s and peak intensities of samples were normalized to that of the silicon wafer at 520  $\text{cm}^{-1}$ . Fluorescence spectra were recorded on an RF-5301PC spectrofluorometer (Shimadzu) and the samples were excited at 488 nm, the bandpass was set at 5 nm for both excitation and emission. Confocal luminescence images were made with a fluorescence optical microscopy (Leica TCS-SP5 scanning confocal microscope), with  $\lambda_{\text{ex}}$  = 488 nm as the excitation source. The static water contact angles were measured at 20  $^{\circ}$ C using a contact angle meter (Data Physics OCA 40) employing drops of 2  $\mu$ L of deionized water. All the measurements were carried out in the same condition.

## RESULTS AND DISCUSSION

Silver NPs stabilized with poly(vinylpyrrolidone) were prepared in ethylene glycol in a large scale via a high-temperature solvothermal method. It was observed that the Ag NPs were about 55 nm with well crystallized, twinned structures (see Figure S1 in the Supporting Information). This particle size was employed based on Boudreau et al report that the plasmonic enhancement efficiency for fluorophores near the surface of Ag NPs reached a maximum for particle sizes in the range 40–70 nm, and the separation distance for highest fluorescence enhancement was  $7 \pm 2$  nm provided by silica spacer between silver nanoparticles and dye in core–shell microspheres. However, ultrathin silica shell (<5 nm) could not be deposited on the silver colloids with sufficient uniformity, hence, whether a thinner spacer would display a greater enhancement or quenching is unknown.<sup>31</sup> Most research on MEF from nanostructured surfaces and single nanoparticles has shown that the fluorophore must be at least 5–10 nm from the metal surface to overcome the surface energy transfer (SET) from the fluorophores to metal NPs,<sup>32</sup> whereas theoretical predictions of the enhancements in hot-spots between nanoparticles showed that the electromagnetic fields were so strong that MEF could efficiently occur even when the fluorophore was just 1–2 nm from the surface. Therefore, there currently exists no reliable experimental method to assist in verifying or in refuting the simulation model.<sup>33,34</sup> In our study, silica spacer with tailored thickness on the nanometer scale was deposited on the surface of Ag NPs via the Stöber sol–gel method. The successful preparation of ultrathin silica shell with a thickness of 3 nm was due to the dilute reaction solution of Ag NPs ( $\sim 1$  mg  $\text{mL}^{-1}$ ), the slow addition of dilute TEOS alcohol solution (9  $\mu\text{L}$   $\text{mL}^{-1}$ ) and rigorous experimental conditions (27  $^{\circ}$ C for 8 h). There particles were almost composed of single particles without aggregates with well-defined dark contrast Ag core and a light and uniform  $\text{SiO}_2$  shell with an average thickness of 3, 8, 18, and 36 nm (Figure 1).

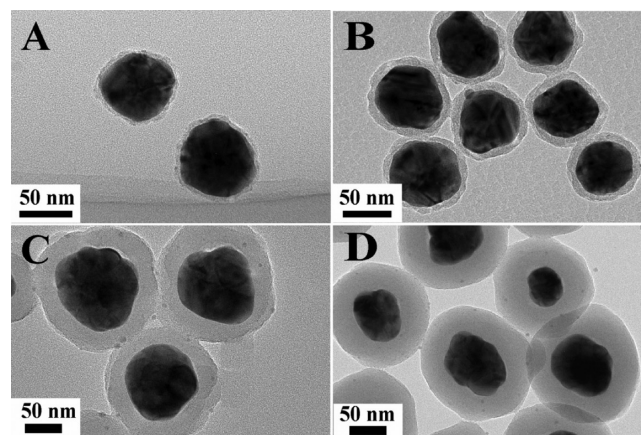


**Figure 1.** TEM images of Ag@first  $\text{SiO}_2$  spacer with the  $\text{SiO}_2$  layer thickness of (A) 3, (B) 8, (C) 18, and (D) 36 nm.

UV–vis absorption spectra (see Figure S2 in the Supporting Information) showed the red shift of surface plasmon resonance peak for silver NPs as the thickness of the silica spacer increases, which was associated with the change of local refractive index.<sup>35</sup> The rise of the extinction below 320 nm was due to the onset of the interband transitions. FiTC, the most

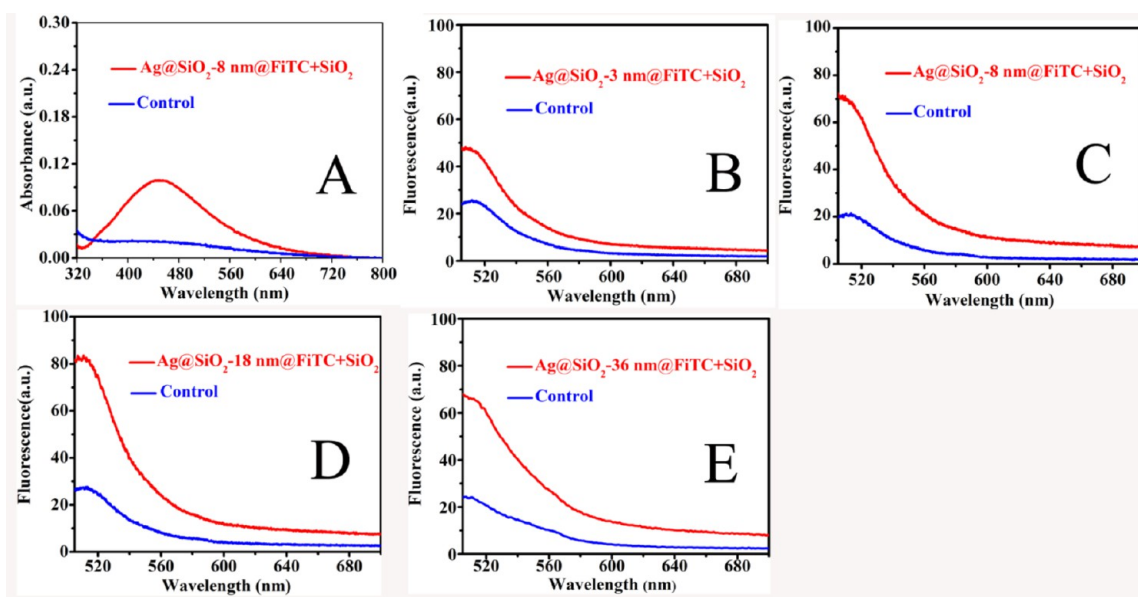


**Figure 2.** (A) UV-vis absorption spectra of representative core-shell Ag@SiO<sub>2</sub>-8 nm @FITC+SiO<sub>2</sub> NPs and the hollow control. (B–E) Fluorescence emission spectra of the Ag@first SiO<sub>2</sub> spacer@FITC+SiO<sub>2</sub> NPs with the silica spacer of (B) 3, (C) 8, (D) 18, and (E) 36 nm and after dissolving the silver core (control). The excitation wavelength was 488 nm.

commonly used fluorophore, was subsequently covalently encapsulated into a thin silica shell ( $\sim 3$  nm) around the first SiO<sub>2</sub> spacer shell, which could not only prevent the dyes from forming aggregates but also improve their photostability. The dye concentration of approximately 8 mM (0.008 mol of FITC per kg of SiO<sub>2</sub>) was adopted on the basis of previous reports,<sup>31</sup> revealing that the relative emission yield reached a maximum at around this concentration and if surpassed, a striking decrease in fluorescence intensity would occur because of the self-quenching of dyes.<sup>36</sup> To confirm the influence of the metal cores on fluorescence emission, control samples (hollow silica nanoshells) were prepared from Ag@first SiO<sub>2</sub> spacer@FITC+SiO<sub>2</sub> fluorescent microspheres. Sodium chloride was employed as an etching agent for Ag core instead of potassium cyanide because of no quenching effect on fluorescence and thus avoided the need for centrifugation and the associated loss of nanoparticles which would result in a larger fluorescence enhancement than actual value. After etching of Ag core, a significant drop of fluorescence intensity simultaneously with the disappearance of the Mie plasmon resonance absorption band of Ag NPs was observed in Figure 2A and the corresponding hollow silica nanoshells were shown in Figure S3a in the Supporting Information. Hydrodynamic diameter measurements were conducted (see Figure S3b in the Supporting Information) and the hydrodynamic diameter of Ag was 141 nm, which was larger than the size measured by the TEM. This is because the PVP ( $M_w = 40\,000$ ) adsorbed on the surface of Ag nanoparticles was swollen in good solvent while it collapsed in the dry state, and the dynamic light scattering (DLS) measurement reflects the particle size in solution, whereas TEM characterization reveals the particle size in dry state.<sup>37</sup> Moreover, the zeta potential of the Ag NPs was  $-8.1$  mV, thus leading to the insufficient colloidal stability and onset of agglomeration, which could also be responsible for the increase in hydrodynamic diameter.<sup>38</sup> After the silica coating, the typical hydrodynamic diameters of Ag@SiO<sub>2</sub>-8 nm@FITC+SiO<sub>2</sub> and Ag@SiO<sub>2</sub>-36 nm@FITC+SiO<sub>2</sub> were ca. 80 and 140 nm, respectively, which were quite close to the size measured

by the TEM. The zeta potentials were  $-32$  and  $-34$  mV, respectively, which means high colloidal stability. After the etching of Ag core, the diameter increased to 152 nm, which is due to some unavoidable agglomeration using NaCl as etching agent.<sup>31</sup> Fluorescence spectra (Figure 2B–E) were employed to investigate the fluorescence enhancement factor (FEF) by calculating the ratios of emission intensities at the most intense peak for Ag@first SiO<sub>2</sub> spacer@FITC+SiO<sub>2</sub> NPs over the corresponding control samples at the same concentration. It was shown that approximately 3.3, 3, 2.7-folds FEF were observed for MEF-2, MEF-3, and MEF-4, respectively, similar to previous reports,<sup>39,40</sup> and it was interesting to note that the fluorescence was still enhanced at about 1.8-fold FEF for MEF-1 with ultrathin silica shell (3 nm), confirming the theory simulation.<sup>33</sup> Herein, we employed the MEF-2 microsphere with the best MEF efficiency for the fabrication of MEF-SERS architecture.

To avoid enormous fluorescence quenching by direct immobilization of Au NPs on fluorescent microspheres, and meanwhile control the thickness of the dielectric SiO<sub>2</sub> layer between Au nanoaggregate and silver NPs to mediate MEF and SERS effects, the MEF-2 microsphere was used as seeding materials to yield the second SiO<sub>2</sub> spacer separating the FITC fluorophore from Au NPs. A modified deposition-precipitation (DP) method was employed to anchor high-density of gold NPs onto the MEF-2 microspheres.<sup>30</sup> Large amount of anionic gold species (e.g.,  $[\text{AuCl}_x(\text{OH})_{4-x}]^-$ ) were formed at  $\text{pH} = 7-8$  adjusted by NaOH solution and optimal for surface nucleation and growth on the positive APTMS modified MEF-2@second SiO<sub>2</sub> spacer microsphere (i.e.,  $\sim 18.0$  mV) by static interaction, potassium-gold solutions were utilized for the further growth of the Au NPs on the microsphere. The high-resolution TEM (HRTEM) image revealed that the second SiO<sub>2</sub> spacers were about 8, 18, 26, 36 nm in thickness and the average size of Au seed was 5 nm (see Figure S4 in the Supporting Information). The representative SEM figure of MEF-2@SiO<sub>2</sub>-26 nm@5 nm-Au seed microspheres demonstrated that these microspheres were uniform (see Figure S5 in the Supporting Information).

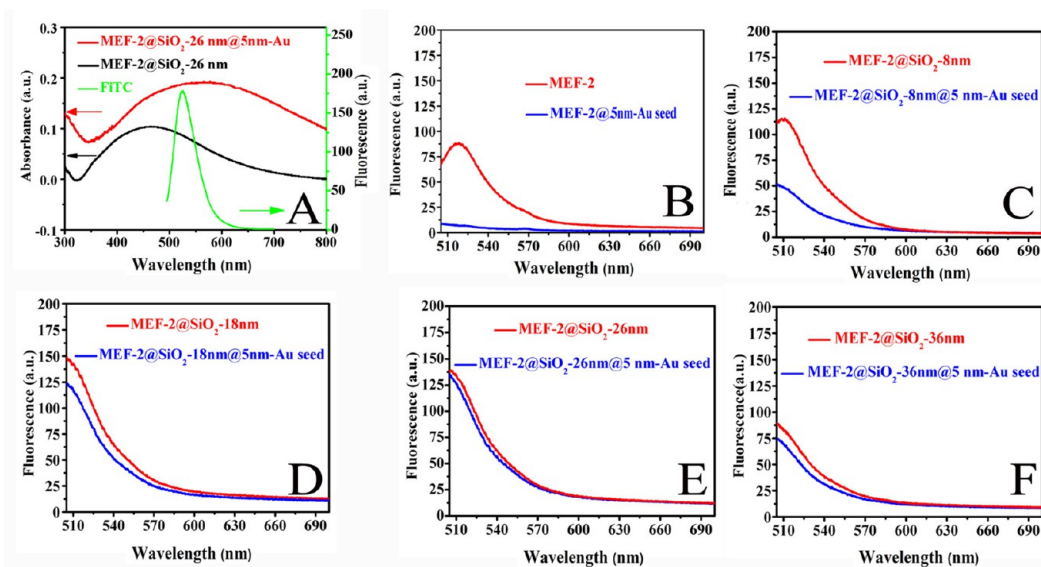


**Figure 3.** (A) Spectral overlap between the excitation spectrum of the FiTC and the plasmon absorption band of Au nanoparticles. (B) Fluorescence emission spectra of MEF-2@5 nm-Au seed, (C) MEF-2@SiO<sub>2</sub>-8 nm@5 nm-Au seed, (D) MEF-2@SiO<sub>2</sub>-18 nm@5 nm-Au seed, (E) MEF-2@SiO<sub>2</sub>-26 nm@5 nm-Au seed, and (F) MEF-2@SiO<sub>2</sub>-36 nm@5 nm-Au seed microspheres.

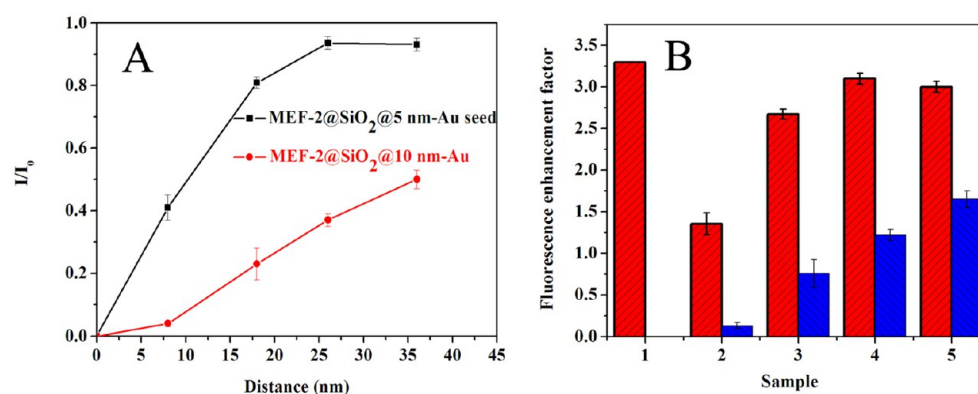


**Figure 4.** (A) Distance-dependent fluorescent emission intensity ratio ( $I/I_0$ ) of MEF-2@second SiO<sub>2</sub> spacer@5 nm-Au seed and MEF-2@second SiO<sub>2</sub> spacer@10 nm Au NPs and (B) the total fluorescent enhancement factor of MEF-2 (sample 1) and FiTC sandwiched between Ag core and Au aggregates before (red histogram) and after (blue histogram) the growth of Au seed on MEF-2@SiO<sub>2</sub>-8 nm (sample 2), MEF-2@SiO<sub>2</sub>-18 nm (sample 3), MEF-2@SiO<sub>2</sub>-26 nm (sample 4), and MEF-2@SiO<sub>2</sub>-36 nm (sample 5) microspheres. The error bars indicate the standard deviations from 3 measurements.

XRD pattern of MEF-2@SiO<sub>2</sub>-26 nm@5 nm-Au seed microspheres was illustrated in Figure S6a in the Supporting Information, which exhibited four characteristic peaks for Au and Ag NPs marked by their indices ((111), (200), (220), and (311)). The peaks indicated that both Ag and Au nanoparticles were in the face-centered cubic (fcc) structure with a good crystallinity although the characteristic peaks for Au and Ag were too close to distinguish. The EDX spectrum further demonstrated the existence of O, Si, Au, and Ag elements (see Figure S6b in the Supporting Information). In general, Au NPs are served as super fluorescence quencher in nanosurface energy transfer (NSET) probes when the size is less than 40 nm because absorption term dominates the extinction spectra and radiative quenching is inevitable. Moreover, according to the NSET method, spectral overlap between Au NPs absorption and fluorophore emission (Figure 3A), and the separation distance which is  $d^{-4}$ -dependent for the energy transfer are the primary reasons for the observed quenching (Figure 3B–F).<sup>41,42</sup>

Thereby, the thickness of the SiO<sub>2</sub> shell was optimized and the emission intensity ratio ( $I/I_0$ ) was determined to investigate the MEF, where  $I_0$  and  $I$  were the emission intensity of MEF-2@second SiO<sub>2</sub> microsphere before and after the deposition of 5 nm Au seed NPs. The results were shown in Figure 4A, revealing that the fluorescence of all of the MEF-2@second SiO<sub>2</sub>@5 nm-Au seed microsphere was partially quenched compared with the emission intensity of MEF-2@second SiO<sub>2</sub> at the same concentration, and the fluorescence quenching was attenuated for the microsphere as the thickness of second silica layers increased from 8 to 36 nm. When the silica thickness reached 26 nm, almost no fluorescence quenching was observed and the fluorescence intensity was ~95% of that for MEF-2@SiO<sub>2</sub>-26 nm, indicating that almost no energy transfer occurred at longer distance between the metal surface and fluorophore. The slight quenching may correlate with the light scattering caused by Au seed. Further increasing the silica layer would promote damping of the surface plasmon band of silver due to the aerial oxidation of Ag in the presence of ammonia by



the Stöber method and dissolution in water as  $\text{Ag}(\text{NH}_3)_2^+$  complexions, resulting in a slightly decrease in emission intensity ratio for MEF-2@SiO<sub>2</sub>-36 nm@5 nm-Au seed than MEF-2@SiO<sub>2</sub>-26 nm@5 nm-Au seed. As the Au seed grew large, the plasmon resonance peak became red-shifted gradually and broadly, which could be characterized by UV–vis absorption spectroscopy (see Figure S7 in the Supporting Information). It was observed that a distinct plasmon resonance peak was no longer observed, instead, a very broad band appeared, extending from near-UV to near-infrared regions, which further verified the formation of a highly dense layer of Au NPs and was similar to the finding made by Kim.<sup>43</sup>

TEM images of MEF-2@ second SiO<sub>2</sub> spacer @Au NPs after the growth of Au seed were shown in Figure 5, it was observed that a high density of Au NPs were deposited on the surface of MEF-2@ second SiO<sub>2</sub> spacer microsphere, and the average size of Au NPs was 10 nm.

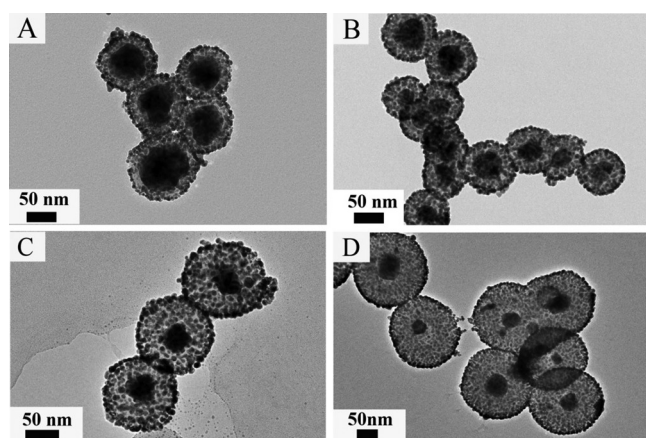


**Figure 5.** TEM images of (A) MEF-2@SiO<sub>2</sub>-8 nm@10 nm-Au, (B) MEF-2@SiO<sub>2</sub>-18 nm@10 nm-Au, (C) MEF-2@SiO<sub>2</sub>-26 nm@10 nm-Au, and (D) MEF-2@SiO<sub>2</sub>-36 nm@10 nm-Au nanoparticles.

Fluorescence emission spectra (Figure 6) were taken to follow the change of fluorescent emission intensity ratio, which were further decreased compared with the corresponding MEF-2@second SiO<sub>2</sub> spacer@5 nm-Au seed microsphere, meaning a worsen fluorescence quenching. Jelani Griffin, et al. reported that Stern–Volmer quenching constant ( $K_{sv}$ ) varies with particle size, as the particle size of Au NPs increased from 5 to 70 nm, The  $K_{sv}$  parameter increased by 3 orders of magnitude from  $4 \times 10^7$  to  $5 \times 10^{10}$ , thus great quenching happened.<sup>41</sup> In our study, when the second silica spacer was 8 nm, fluorescence was greatly quenched. While separated at longer distance, the emission intensity ratios of MEF-2@second SiO<sub>2</sub> spacer@10 nm-Au NPs were increased (Figure 4A); however, they were still lower than that of MEF-2@second SiO<sub>2</sub> spacer@5 nm-Au seed NPs, which could be explained taking into account two factors. First, when the size of Au NPs was lower than 15 nm, the slight change of size will affect the  $K_{sv}$  parameter little. Fluorophore located in the range that NEST could efficiently occur will suffer from less quenching after the growth of Au seed. As light scattering was proportional to the scattering cross-section ( $C_{sca}$ ), and  $C_{sca}$  was square of the radius of the spherical particle dependent.<sup>44</sup> Thus, the improvement of energy transfer and light scattering caused by the enlarged size jointly make an effect on the further fluorescence quenching. Second, as the separation distance

between Au NPs and fluorophores further increased (>18 nm), the energy transfer efficiency attenuated greatly and light scattering made a dominant contribution to the fluorescence quenching. Large Au NPs would scatter more light than the 5 nm Au seed, resulting in less incident light arriving at the surface of Ag NPs to induce plasmon resonance with fluorophore. We calculated the total fluorescence enhancement factor (TFET) coupling the fluorescence quenching caused by Au NPs with fluorescence enhancement from Ag core according to the following relation, and the results are shown in Figure 4B.

$$\text{TFET} = 3.3I/I_0 \quad (1)$$

They were about 0.13, 0.75, 1.22, and 1.65-fold TFET for MEF-2@SiO<sub>2</sub>-8 nm@10 nm-Au, MEF-2@SiO<sub>2</sub>-18 nm@10 nm-Au, MEF-2@SiO<sub>2</sub>-26 nm@10 nm-Au, and MEF-2@SiO<sub>2</sub>-36 nm@10 nm-Au microspheres, respectively.

Considering that the larger Au particles aggregation on the surface of the microsphere will provide much higher enhancement of electromagnetic field. The MEF-2@SiO<sub>2</sub>-36 nm@10 nm-Au nanoaggregate microspheres could be used as efficient SERS-active substrates. We thus evaluated their performance by using 4-ABT as the model SERS reporter. To explore the homogeneity and reproducibility of the SERS signal, we measured SERS spectra at 10 randomly selected spots in one address on the sample. As shown in Figure 7A, the feature peaks of 4-ABT at 1572, 1433, 1390, 1137, and 1068  $\text{cm}^{-1}$  were observed and agreed well with literature values.<sup>45</sup> Raman peaks of 4-ABT also appeared in SERS spectra even if concentrations of 4-ABT solution decreased to  $1 \times 10^{-7}$ . The enhancement factors (EF) could be calculated by the following equation

$$\text{EF} = (I_{\text{SERS}}/I_{\text{Raman}})(N_{\text{bulk}}/N_{\text{ads}}) \quad (2)$$

Where  $I_{\text{SERS}}$  and  $I_{\text{Raman}}$  are the band intensity of the selected band at 1572  $\text{cm}^{-1}$  ( $\nu_{8a}$ ) obtained by SERS and the corresponding band intensity of the bulk solution. The  $N_{\text{bulk}}$  and  $N_{\text{ads}}$  are the numbers of molecules from the bulk solution and molecules adsorbed on the microsphere in the cross-section of laser beam, respectively. As the characterization was conducted on the same Raman spectrometer,  $N_{\text{bulk}}$  and  $N_{\text{ads}}$  may be replaced by the concentrations of the bulk and SERS solution, respectively.<sup>46</sup> The EF for the SERS detection of 4-ABT in our experiment was calculated to be  $7 \times 10^6$  for MEF-2@SiO<sub>2</sub>-36 nm@10 nm-Au under optimal experiment condition. The enhancement factor was found to increase when the second silica shell thickness was increased from 8 to 36 nm (Figure 7B). To demonstrate that the interior Ag core was indeed helping in enhancing the Raman signal, the control sample (SiO<sub>2</sub>@Au nanoparticles) of similar size without a silver core was synthesized<sup>47</sup> and characterized by TEM (see Figure S8 in the Supporting Information). As shown in Figure 7C, it was found that the detection limit of SiO<sub>2</sub>@Au could only reach  $1 \times 10^{-5}$  M, and even at this concentration, the EF of MEF-2@SiO<sub>2</sub>-36 nm@10 nm-Au was about three times higher than that of SiO<sub>2</sub>@Au nanoparticle. As a conclusion, it was estimated that the enhancement factor of MEF-2@SiO<sub>2</sub>-36 nm@10 nm-Au was 300-fold larger than that at the absence of Ag core. As shown in Scheme 1B, we proposed that as the favorable incident light could still reach the surface of Ag NPs to induce MEF, they underwent multiple reflections at the upper and lower surfaces of the dielectric SiO<sub>2</sub> layer before emerging from the gap between the Au NPs, and the regions where the incident and refracted light constructively interfered

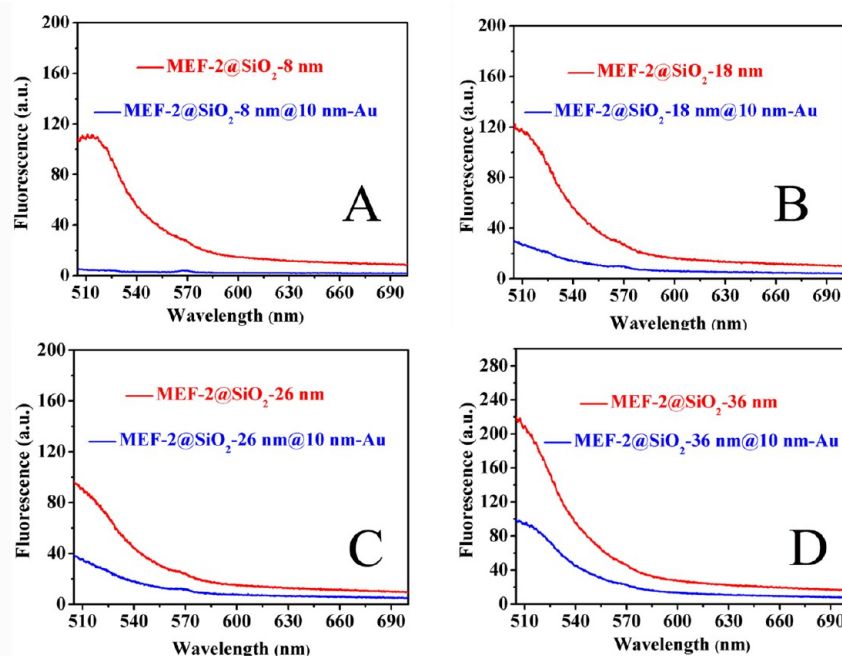


**Figure 6.** Fluorescence emission spectra of (A) MEF-2@SiO<sub>2</sub>-8 nm@10 nm-Au, (B) MEF-2@SiO<sub>2</sub>-18 nm@10 nm-Au, (C) MEF-2@SiO<sub>2</sub>-26 nm@10 nm-Au and (D) MEF-2@SiO<sub>2</sub>-36 nm@10 nm-Au microspheres.

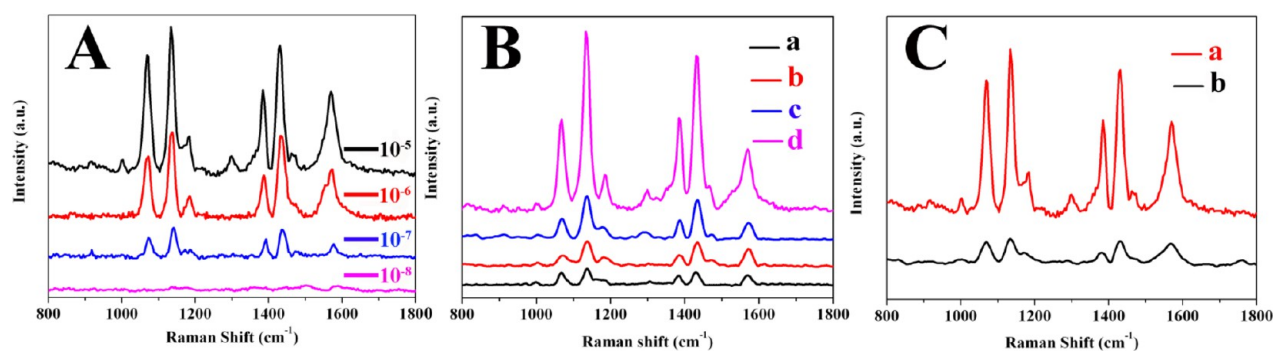


**Figure 7.** (A) Raman spectra for MEF-2@SiO<sub>2</sub>-36 nm@10 nm-Au composite microspheres with various 4-ABT concentrations; (B) Raman spectra of 10<sup>-7</sup> M 4-ABT adsorbed on the surface of (a) MEF-2@SiO<sub>2</sub>-8 nm@10 nm-Au NPs, (b) MEF-2@SiO<sub>2</sub>-18 nm@10 nm-Au NPs, (c) MEF-2@SiO<sub>2</sub>-26 nm@10 nm-Au NPs, and (d) MEF-2@SiO<sub>2</sub>-36 nm@10 nm-Au nanoparticles; (C) Raman spectra of 1 × 10<sup>-5</sup> M 4-ABT adsorbed on the surface of (a) MEF-2@SiO<sub>2</sub>-36 nm@10 nm-Au and (b) the control sample (SiO<sub>2</sub>@Au).

(satisfying Bragg's condition) would make the field intensity at that point amplified. Raman reporters presented in such regions would experience an increased electric field, and hence, higher Raman intensity was observed. Moreover, the surface plasmon coupling between the gold nanoaggregate on the surface would also have a strong contribution to the enhancement of the Raman signal. Finally, the two factors collectively made a critical contribution to the interference and surface coenhanced Raman scattering. This was in some way similar to Min et al.'s<sup>28</sup> report that using silver nanoprisms on top of a gold ground plane spaced by a TiO<sub>2</sub> dielectric layer to coherently enhance the SERS signal of rhodamine 6G with more than 50-fold SERS enhancement.

To gain insight into the effect of new architecture as sensitive SERS labels, we further carried out a multiplex encoding experiment. MEF-2@SiO<sub>2</sub>-26 nm@10 nm-Au microsphere was employed because of its stable Ag core as above-mentioned. Figure 8A showed the SERS spectra of five different Raman reporters adsorbed onto MEF-2@SiO<sub>2</sub>-26 nm@10 nm-Au NPs

substrates and the arrows marked the unique fingerprint peaks obtained which could be utilized for the creation of a large number of Raman encodings by employing an appropriate combination of different reporters (see Table S1 in the Supporting Information). For instance, when two kinds of Raman label compounds, such as 4-methylbenzenethiol (4-MT) and 2-naphthalenethiol (2-NT), were mixed at different molar ratios (4-MT:2-NT, 3:1, 7:1, 12:1, 19:1, 39:1), the unique peaks for multiplex tagging of each reporter (4-MT, 794 cm<sup>-1</sup>; 2-NT, 769 cm<sup>-1</sup>) could be clearly resolved in terms of their Raman shift and intensity (Figure 8B). Many other Raman-label reporters could be used in such combinations with strong SERS signals. Although, in principle, abundant codes could be obtained by using different kinds of SERS reporters, the preparation process would get rather complicated or even impractical because of the problems of spectral overlap or limited available types of agents. Nevertheless, in our work, the number of codes could be enlarged much easily and more feasible in actual application due to the MEF and SERS dual-



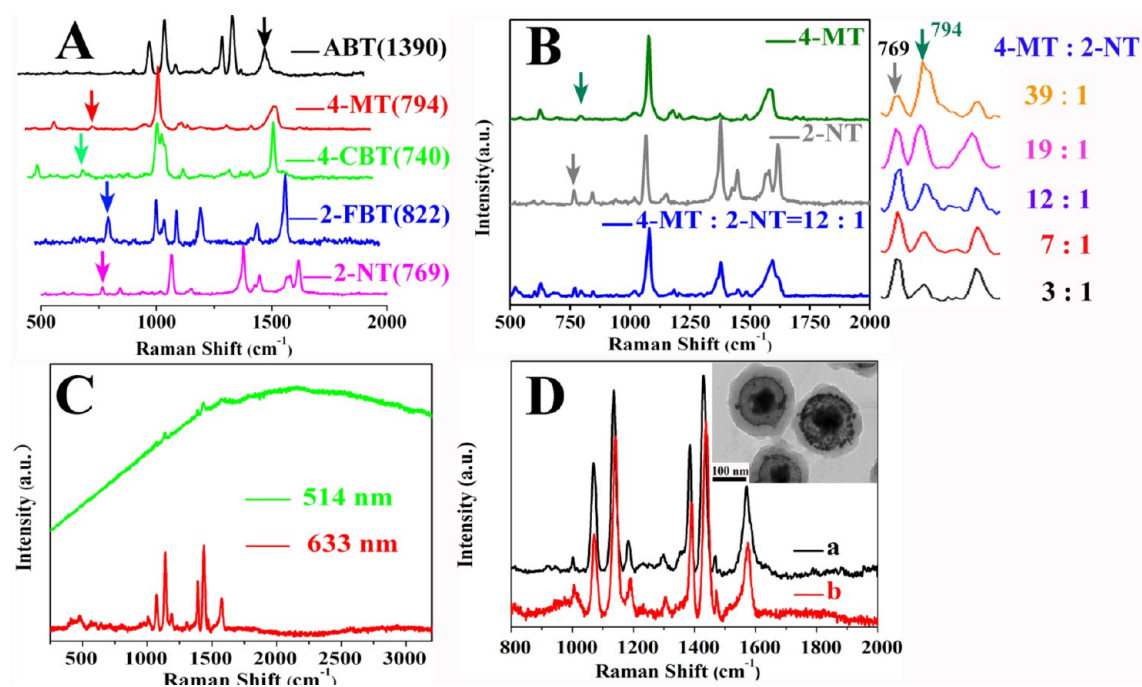
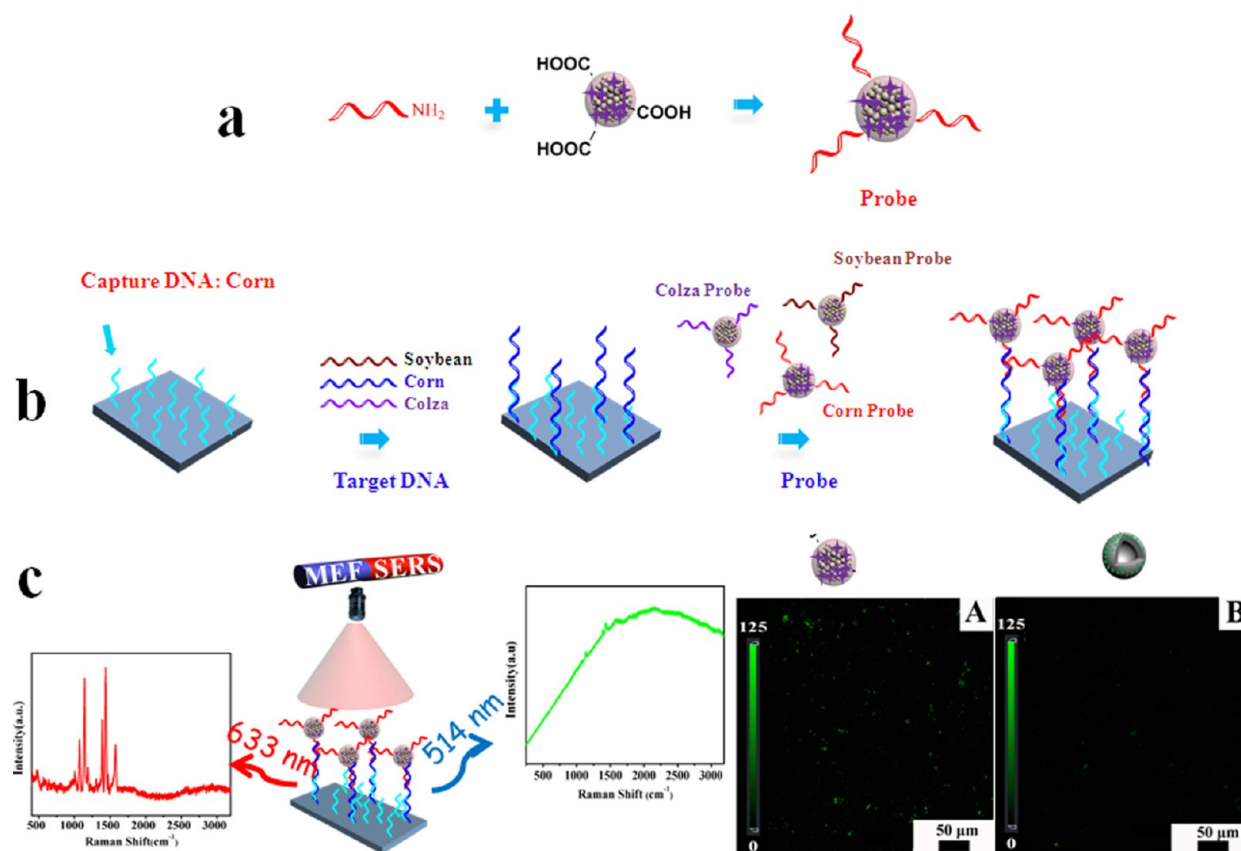


**Figure 8.** Raman spectra of (A) five different kinds of Raman label compounds (ABT, 4-MT, 4-CBT, 2-FBT, 2-NT) and (B) a combination of 4-MT and 2-NT with different molar ratios (4-MT:2-NT, 3:1, 7:1, 12:1, 19:1, 39:1) obtained by using MEF-2@SiO<sub>2</sub>-26 nm@10 nm-Au as SERS-active substrate. (C) Raman spectra taken from MEF-2@SiO<sub>2</sub>-26 nm@10 nm-Au @SiO<sub>2</sub> microspheres using 514 and 633 nm radiation as the excitation source. (D) Raman spectra obtained from 4-ABT on (a) MEF-2@SiO<sub>2</sub>-26 nm@10 nm-Au and (b) MEF-2@SiO<sub>2</sub>-26 nm@10 nm-Au @SiO<sub>2</sub> microspheres. Inset: TEM image of MEF-2@SiO<sub>2</sub>-26 nm@10 nm-Au @SiO<sub>2</sub> composite microspheres.

#### Scheme 2. Process of Multiplex DNA Sequence Detection of Genetically Modified Organisms (GMO) Using MEF-SERS Nanobarcodes



mode encoding strategy, the fluorescence from FITC and SERS signals were separately generated by switching the wavelength of the excitation light from 514 to 633 nm (Figure 8C), a one-shot brightest fluorescence image over a large area of specimen greatly facilitated the further deep-insight SERS analysis. Additionally, different kinds of fluorescent agents and SERS analytes were conjugated onto two different layers in the new architecture, and there was no energy transfer between fluorescence and SERS signals. Thus, the problem of spectral overlap was alleviated, allowing for more spectrally distinct codes.

**Multiplex DNA Sequence Detection of Genetically Modified Organisms (GMO) Using MEF-SERS Nanobarcodes.** Nowadays, the safety of genetically modified organisms has aroused universal controversy about ecological risk, environmental problems, and human health. It is of vital importance to identify novel methods for the detection of inserted exogenous genes of GMOs. To demonstrate the application of the dual-mode MEF-SERS microsphere for multiplex DNA sequence detection of GMO, we performed a proof-of-concept chip-based DNA sandwich hybridization assay based on the sandwichlike assembly of three oligonucleotides that is commonly used in the detection of nonlabeled target DNAs: half of the target DNA strand is hybridized (i.e., forms a duplex) with capture DNA on the chip and the other half strand of the target DNA is hybridized with probe DNA on the nanoparticle. We designed three types of specific oligonucleotides as the detection targets from GMO,<sup>48</sup> including GMO corn NK 603, GMO colza RT73, GMO soybean GTS 40–3–2. The nucleotide sequences in details were illustrated in Table S2 in the Supporting Information.

As shown in Scheme 2, we first coated MEF-SERS microspheres with a layer of inert and biocompatible silica encapsulating fluorophore and SERS analytes in one unit, denominated as MEF-SERS nanobarcode. Recent reports have shown that thin silica shells prepared by the Stöber method were usually porous, and that the resulting pore size tended to increase with increasing ammonia concentration, which would allow small molecules and ions to penetrate and react with the core.<sup>49</sup> Specifically, it was reported that SERS tags with 15 nm silica shell, external dyes could penetrate the shell and adsorb onto the Au NPs surface. Conversely, thicker silica shells (e.g., 20 nm) could effectively block the penetration of external dye molecules.<sup>50</sup> In our study, the thickness of silica coating was ca. 30 nm (Figure 8D, inset), and Raman intensity of analyte molecules (4-ABT) before and after encapsulation with outer silica shells almost remained unchanged, suggesting nearly no loss of 4-ABT molecules during silica coating due to the strong complexation of 4-ABT thiol groups to Au nanoparticles and a higher transmission of light at a thinner organosilica shell (compared with the silica spacer thickness of 55 nm<sup>51</sup>). As we know, silica shell could shield the nanoparticle interior components from the exterior environment. Therefore, interference from external compounds could be avoided. For instance, when MEF-SERS nanobarcode was treated with R6G, the SERS signals originated exclusively from 4-ABT (data are not shown here), no characteristic peaks of R6G were observed at all.

Subsequently, the MEF-SERS nanobarcodes were COOH-modified to facilitate the conjugation of probe DNA to the surface. FTIR spectra provided clear evidence for the preparation procedure of the COOH-modified MEF-SERS nanobarcodes (see Figure S9 in the Supporting Information).

Concomitant with the APTMS-modified MEF-SERS nanobarcodes, two IR bands at 3298 cm<sup>-1</sup> and 3198 cm<sup>-1</sup> are due to the asymmetric and symmetric NH<sub>2</sub> stretching. The band at 1585 cm<sup>-1</sup> is attributed to N–H asymmetric bending vibration, additionally, the characteristic antisymmetric and symmetric CH<sub>2</sub> stretches, typically at 2925 cm<sup>-1</sup> and 2850 cm<sup>-1</sup> and the methyl stretching at 2959 cm<sup>-1</sup> were also readily seen. After reacting with succinic anhydride, a broad absorption band at around 3450 cm<sup>-1</sup> corresponded to the O–H stretching vibration, and several new adsorption peaks appeared at 1636 and 1728 cm<sup>-1</sup>, which could be assigned to the C=O stretching vibration in the amide group and the C=O stretching vibration in the carboxyl group, respectively. Thereby, the surface of MEF-SERS nanobarcodes was successfully modified with COOH groups. This was also confirmed by the zeta potential characterization. As the existence of silanol groups on MEF-SERS nanobarcodes, the zeta potential of microsphere was –30.0 mV. After the functionalization with amino groups, the zeta potential of APTMS-modified MEF-SERS nanobarcodes was increased to 18.4 mV, and then decreased to –29.4 mV for the COOH-modified MEF-SERS nanobarcodes. Next, the NH<sub>2</sub>-probe oligonucleotide was covalently attached to nanobarcodes with COOH via EDC and Sulfo-NHS. It was observed that new peaks corresponding P–O bending modes appeared around 600 and 560 cm<sup>-1</sup> in the IR spectra, meanwhile, the peak at 1728 cm<sup>-1</sup> gradually disappeared. EDX analysis also confirmed the existence of P group derived from DNA linking to the MEF-SERS nanobarcodes (see Figure S10 in the Supporting Information). The zeta potential of NH<sub>2</sub>-probe oligonucleotide was –13.0 mV. When the NH<sub>2</sub>-probe oligonucleotide was grafted to COOH-modified MEF-SERS nanobarcodes by the succinimide coupling method, the zeta potential of probe DNA-functionalized MEF-SERS nanobarcodes was increased to a value of –15.0 mV because of the graft of less negatively charged probe oligonucleotide compared with the COOH-modified MEF-SERS nanobarcodes. A control was conducted that COOH-modified MEF-SERS nanobarcodes were directly mixed with probe DNA (soybean) without EDC and NHS coupling, it was found that after grafted with probe DNA through EDC and NHS coupling, the plasmon peak shifted from 535 to 541 nm (see Figure S11 in the Supporting Information). The red shift in plasmon peak value was due to the change in dielectric constant of the media surrounding the MEF-SERS nanobarcode because of the DNA linkage. Meanwhile, DNA-modified MEF-SERS nanobarcode showed much stronger absorbance at 260 nm comparing with the control due to the DNA absorption maximum at 260 nm. We also measured the supernatant solutions after centrifugation of DNA-modified MEF-SERS and the control, and it is shown that after thoroughly washed, the remained probe DNA existing in the solution for DNA-modified MEF-SERS was lower than the control, which indicated the successful immobilization of probe DNA onto the nanobarcodes. The particle concentration of the colloidal solution was obtained from the determination of elemental Ag by flame atomic absorption spectrometry (Ag concentration: 0.06 mg/mL), and the mass of single Ag NP with an average diameter of 55 nm was  $9.135 \times 10^{-16}$  g, thus the particle concentration of the colloidal solution is  $6 \times 10^5$ /mL, and the density of oligonucleotides on the surface of MEF-SERS nanobarcode was calculated to be 258/particle.

Following the fabrication of probe DNA marked by MEF-SERS nanobarcode in the sandwich structure, the capture DNA

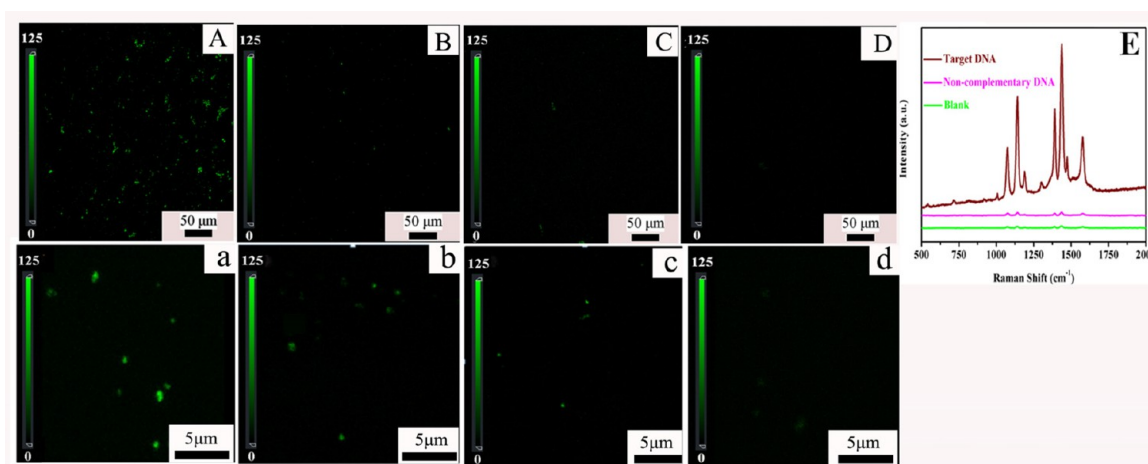


**Figure 9.** Confocal luminescence images with different magnification of DNA hybridization assay for (A, a) target DNA, (B, b) noncomplementary DNA, (C, c) a blank solution, and (D, d) hollow silica nanoshells of MEF-2, and (E) SERS spectra of DNA hybridization assay.

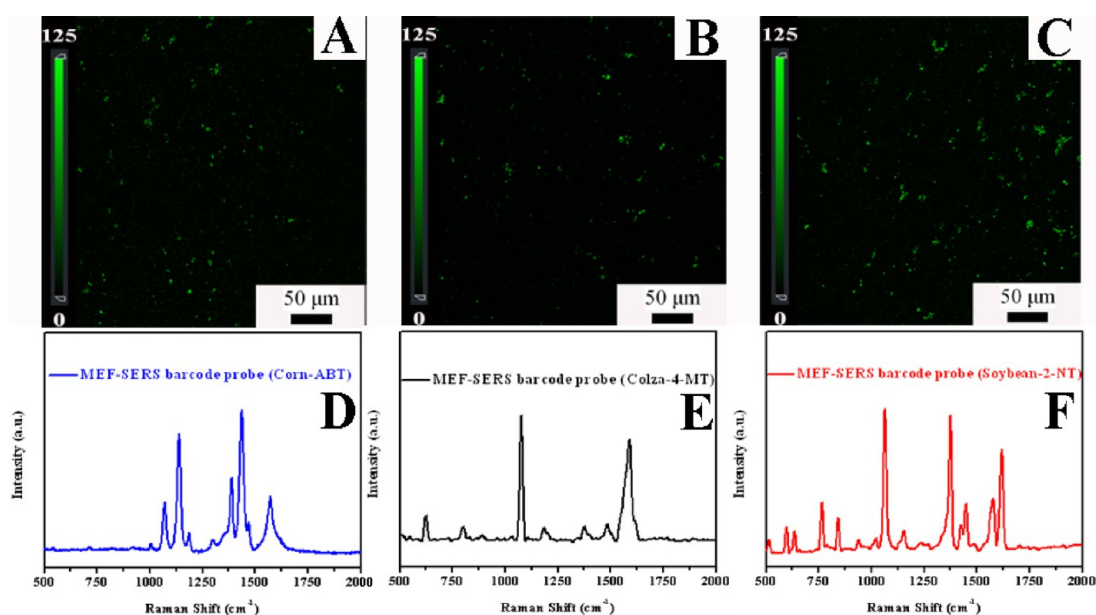


**Figure 10.** Confocal luminescence images and SERS spectra of (A, D) Capture DNA-1 (glass slide-1), (B, E) Capture DNA-2 (glass slide-2) and (C, F) Capture DNA-3 (glass slide-3) after incubation in a mixed DNA solution and mixed MEF-SERS nanobarcode solution.

was immobilized on the glass chip. The surface of the glass slide was treated with piranha solution and grafted with GPTMS, and capture DNA strands with amino group were immobilized on the substrate through the coupling reaction between epoxy groups and amino groups.  $\text{NaBH}_4$ , a common used reducing agent, was employed to reduce uncoupled epoxy groups from nonspecific binding of DNA. Contact-angle measurements were employed to confirm the successful modification (see Figure S12 in the Supporting Information). The contact angles of piranha-solution-treated and GPTMS-grafted substrates were 46 and 68 °C, respectively, whereas capture DNA conjugated substrate showed a lower contact angle of 43 °C because of the presence of many phosphate groups along the DNA chain.<sup>52</sup> Subsequently, the target DNA strands and probe DNA-marked by MEF-SERS nanobarcode were by turn incubated with the substrate by the interaction between complementary sequences to form a sandwich hybridization structure. In the preliminary experiment, we checked the ability of MEF-SERS microbarcodes employing ABT as SERS analyte to detect target

DNA from GMO corn NK 603 in complementary DNA (target DNA), control DNA (noncomplementary sequences, target DNA of GMO soybean GTS 40–3–2) and a blank solution, respectively. Laser confocal scanning microscopy (LCSM) imaging with different magnification is shown in Figure 9A–C and a–c. Intense fluorescence signals resulting from the presence of target DNA are clearly shown, whereas for the noncomplementary DNA, negligible signals were detectable, and for a blank solution, almost no fluorescence signal could be detected.

Meanwhile, the noticeable difference in the brightness of the emission spots provided unambiguous information on enhanced fluorescence emission in the presence of silver cores (Figure 9D, d) comparing with Figure 9a–c. Moreover, a deep analysis by SERS experiments further confirmed the specific hybridization assay of the MEF-SERS nanobarcode- $s_{4\text{-ABT}}$  in the presence of the target DNA (Figure 9E), which indicate a high degree of sequence specificity and a low level of nonspecific adsorption.



As shown in Table S2 in the Supporting Information, three different types of MEF-SERS nanobarcode probes were selected for multiplex DNA sequence detection of GMO in a mixed target DNA solution (the procedure was showed in Scheme 2b). First, three modified glass slides were bound with capture DNAs of GMO corn NK 603 (glass slide-1), GMO colza RT73 (glass slide-2), and GMO soybean GTS 40–3–2 (glass slide-3), respectively, followed by sequential incubation in a mixture solution of the three target DNA strands of the above GMO and a mixture solution of the three MEF-SERS nanobarcode-probes (MEF-SERS-nanobarcode<sub>ABT</sub>-corn probe, MEF-SERS-nanobarcode<sub>4-MT</sub>-colza probe, and MEF-SERS-nanobarcode<sub>2-NT</sub>-soybean probe in Table S2 in the Supporting Information). The concentration of each kind of target DNA strands was kept at a fixed amount of  $10 \mu\text{L} \times 1 \mu\text{M}$  for all the experiments, and the hybridization conditions were the same as above-mentioned. LCSM imaging and SERS spectra recorded from each glass slide were shown in Figure 10. Obviously, each SERS spectrum only displayed the unique spectroscopic signals of the corresponding nanobarcode-probe, which meant no cross talk between different target DNA and nanobarcode-probe, and the specific target DNA strands could be easily and uniquely assayed according to the “fingerprint” of MEF-SERS nanobarcode-probes. Therefore, these MEF-SERS nanobarcode-probes hold great potential in the fast, specific, and selective assay of biomolecules in complex biological systems.

## CONCLUSION

In summary, a new strategy to efficiently enhance fluorescence and further enhance SERS was developed on the basis of Ag@first SiO<sub>2</sub> spacer@FiTC+SiO<sub>2</sub>@second SiO<sub>2</sub> spacer@Au nanoaggregate concentric multilayer core–shell nanostructures with a tunable thickness of silica spacer. The straightforward origin of the observed MEF-SERS effect in the core–shell unit, which gives rise to 1.6-fold fluorescence enhancement factor and additional 300-fold enhanced SERS, is due to the optical modulation of the plasmonic metallic surface of interior Ag NPs. These interior Ag NPs are not only combined with a fluorophore to form a plasmophore for fluorescence enhancement but also act as scattering antennae that reflect incident light into the confined region, so-called hot spots, sandwiched by the Au nanoaggregate surface and collectively leading to a further significant enhancement of SERS. We have shown initial proof-of-concept experiments to exemplify their advantages, using probe DNA-modified MEF-SERS-nanobarcode to detect target DNA strands, which exhibited good specificity and sensitivity for the target DNA. It can be expected that the MEF-SERS composite substrate has the potential to improve sensing for a large group of analyte molecules and to aid the development of chemically specific SERS-based sensors.

## ASSOCIATED CONTENT

### Supporting Information

Experimental process of etching Ag core of Ag@first SiO<sub>2</sub> spacer@SiO<sub>2</sub>-FiTC microspheres (control sample). TEM images of Ag NPs, MEF-2@SiO<sub>2</sub>@Au seed, SiO<sub>2</sub>@Au, and the hollow control. Table of spectroscopic fingerprints of each type of MEF-SERS barcodes and nucleotide sequences of GMOs target, probes, and captures used for the experiments. SEM image, X-ray diffraction pattern, and EDX spectrum of MEF-2@SiO<sub>2</sub>-26 nm@Au core–shell microspheres, FT-IR spectra of DNA-modified MEF-SERS nanobarcode, contact angles of substrates, UV–vis absorption spectra of Ag@

SiO<sub>2</sub> NPs with different spacer thickness, MEF-2@SiO<sub>2</sub>-8 nm@10 nm-Au, MEF-2@SiO<sub>2</sub>-18 nm@10 nm-Au, MEF-2@SiO<sub>2</sub>-26 nm@10 nm-Au, MEF-2@SiO<sub>2</sub>-36 nm@10 nm-Au, DNA-modified MEF-SERS nanobarcode, the control, the supernatant solutions after centrifugation of DNA-modified MEF-SERS nanobarcode reaction solution, and the supernatant solutions after centrifugation of the control solution. This material is available free of charge via the Internet at <http://pubs.acs.org/>.

## AUTHOR INFORMATION

### Corresponding Author

\*E-mail: peiyiwu@fudan.edu.cn. Tel: +86-21-65643255. Fax: +86-21-65640293.

### Notes

The authors declare no competing financial interest.

## ACKNOWLEDGMENTS

This work was financially supported by the National Basic Research Program of China (2009CB930000).

## REFERENCES

- (1) Li, X.; Choy, W. C. H.; Huo, L.; Xie, F.; Sha, W. E. I.; Ding, B.; Guo, X.; Li, Y.; Hou, J.; You, J.; Yang, Y. *Adv. Mater.* **2012**, *24*, 3046.
- (2) Kim, J.; Koh, J. K.; Kim, B.; Kim, J. H.; Kim, E. *Angew. Chem., Int. Ed.* **2012**, *51*, 6864.
- (3) Zheng, Z.; Huang, B.; Qin, X.; Zhang, X.; Dai, Y. J. *Mater. Chem.* **2011**, *21*, 9079.
- (4) Zhou, L.; Ding, F.; Chen, H.; Ding, W.; Zhang, W.; Chou, S. Y. *Anal. Chem.* **2012**, *84*, 4489.
- (5) Taylor, A. B.; Kim, J.; Chon, J. W. M. *Opt. Express* **2012**, *20*, 5069.
- (6) Dasary, S. S. R.; Singh, A. K.; Senapati, D.; Yu, H.; Ray, P. C. J. *Am. Chem. Soc.* **2009**, *131*, 13806.
- (7) Zhang, Y.; Hong, H.; Myklejord, D. V.; Cai, W. *Small* **2011**, *7*, 3261.
- (8) Auchincloss, C. A. R.; Richardson, P.; McGuinness, C.; Mallikarjun, V.; Donaldson, K.; McNab, H.; Campbell, C. J. *ACS Nano* **2011**, *6*, 888.
- (9) Serra, A.; Manno, D.; Filippo, E.; Buccolieri, A.; Urso, E.; Rizzello, A.; Maffia, M. *Sens. Actuators, B* **2011**, *156*, 479.
- (10) Yigit, M. V.; Zhu, L.; Ifediba, M. A.; Zhang, Y.; Carr, K.; Moore, A.; Medarova, Z. *ACS Nano* **2010**, *5*, 1056.
- (11) Banholzer, M. J.; Millstone, J. E.; Qin, L.; Mirkin, C. A. *Chem. Soc. Rev.* **2008**, *37*, 885.
- (12) Grzelczak, M.; Perez Juste, J.; Mulvaney, P.; Liz-Marzan, L. M. *Chem. Soc. Rev.* **2008**, *37*, 1783.
- (13) Tian, J. H.; Liu, B.; Yang, Z. L.; Ren, B.; Wu, S. T.; Tao, N.; Tian, Z. Q. *J. Am. Chem. Soc.* **2006**, *128*, 14748.
- (14) Bowen, A. M.; Motala, M. J.; Lucas, J. M.; Gupta, S.; Baca, A. J.; Mihi, A.; Alivisatos, A. P.; Braun, P. V.; Nuzzo, R. G. *Adv. Funct. Mater.* **2012**, *22*, 2927.
- (15) Zhou, Q.; Zhang, X.; Huang, Y.; Li, Z.; Zhao, Y.; Zhang, Z. *Appl. Phys. Lett.* **2012**, *100*, 113101.
- (16) Li, J. M.; Wei, C.; Ma, W. F.; An, Q.; Guo, J.; Hu, J.; Wang, C. C. *J. Mater. Chem.* **2012**, *22*, 12100.
- (17) Bu, Y.; Lee, S. *ACS Appl. Mater. Inter.* **2012**, *4*, 3923.
- (18) Liusman, C.; Li, H.; Lu, G.; Wu, J.; Boey, F.; Li, S. Z.; Zhang, H. *J. Phys. Chem. C* **2012**, *116*, 10390.
- (19) Qin, L. D.; Zou, S. L.; Xue, C.; Atkinson, A.; Schatz, G. C.; Mirkin, C. A. *Proc. Natl. Acad. Sci. U. S. A.* **2006**, *103*, 13300.
- (20) Chen, A.; DePrince, A. E.; Demortière, A.; Joshi-Imre, A.; Shevchenko, E. V.; Gray, S. K.; Welp, U.; Vlasko-Vlasov, V. K. *Small* **2011**, *7*, 2365.
- (21) Sánchez González, A.; Corni, S.; Mennucci, B. *J. Phys. Chem. C* **2011**, *115*, 5450.

- (22) Liu, H.; Zhang, L.; Lang, X.; Yamaguchi, Y.; Iwasaki, H.; Inouye, Y.; Xue, Q.; Chen, M. *Sci. Rep.* **2011**, *1*, 1.
- (23) Tao, C. a.; Zhu, W.; An, Q.; Yang, H.; Li, W.; Lin, C.; Yang, F.; Li, G. *J. Phys. Chem. C* **2011**, *115*, 20053.
- (24) Akselrod, G. M.; Walker, B. J.; Tisdale, W. A.; Bawendi, M. G.; Bulovic, V. *ACS Nano* **2011**, *6*, 467.
- (25) Liu, Y.; Xu, S.; Li, H.; Jian, X.; Xu, W. *Chem. Commun.* **2011**, 3784.
- (26) Mubeen, S.; Zhang, S.; Kim, N.; Lee, S.; Krämer, S.; Xu, H.; Moskovits, M. *Nano Lett.* **2012**, *12*, 2088.
- (27) Gao, L.; Ren, W.; Liu, B.; Saito, R.; Wu, Z.-S.; Li, S.; Jiang, C.; Li, F.; Cheng, H. M. *ACS Nano* **2009**, *3*, 933.
- (28) Min, Q. A.; Pang, Y. J.; Collins, D. J.; Kuklev, N. A.; Gottselig, K.; Steuerman, D. W.; Gordon, R. *Opt. Express* **2011**, *19*, 1648.
- (29) Zhang, F.; Braun, G. B.; Shi, Y.; Zhang, Y.; Sun, X.; Reich, N. O.; Zhao, D.; Stucky, G. *J. Am. Chem. Soc.* **2010**, *132*, 2850.
- (30) Phonthammachai, N.; Kah, J. C. Y.; Jun, G.; Sheppard, C. J. R.; Olivo, M. C.; Mhaisalkar, S. G.; White, T. J. *Langmuir* **2008**, *24*, 5109.
- (31) Lessard Viger, M.; Rioux, M.; Rainville, L.; Boudreau, D. *Nano Lett.* **2009**, *9*, 3066.
- (32) Guerrero, A. R.; Aroca, R. F. *Angew. Chem., Int. Ed.* **2011**, *50*, 665.
- (33) Le Ru, E. C.; Etchegoin, P. G.; Grand, J.; Félidj, N.; Aubard, J.; Lévi, G. *J. Phys. Chem. C* **2007**, *111*, 16076.
- (34) Gill, R.; Le Ru, E. C. *Phys. Chem. Chem. Phys.* **2011**, *13*, 16366.
- (35) Tang, F.; He, F.; Cheng, H.; Li, L. *Langmuir* **2010**, *26*, 11774.
- (36) Imhof, A.; Megens, M.; Engelberts, J. J.; de Lang, D. T. N.; Sprik, R.; Vos, W. L. *J. Phys. Chem. B* **1999**, *103*, 1408.
- (37) Ma, W.; Xu, S.; Li, J.; Guo, J.; Lin, Y.; Wang, C. *J. Polym. Sci., Part A: Polym. Chem.* **2011**, *49*, 2725.
- (38) Rivera-Gil, P.; Jimenez De Aberasturi, D.; Wulf, V.; Pelaz, B.; Del Pino, P.; Zhao, Y.; De La Fuente, J. M.; Ruiz De Larramendi, I.; Rojo, T.; Liang, X. J.; Parak, W. J. *Acc. Chem. Res.* **2012**, *46*, 743–749.
- (39) Liu, J.; Li, A.; Tang, J.; Wang, R.; Kong, N.; Davis, T. P. *Chem. Commun.* **2012**, 48, 4680.
- (40) Cheng, D.; Xu, Q. H. *Chem. Commun.* **2007**, 0, 248.
- (41) Griffin, J.; Singh, A. K.; Senapati, D.; Rhodes, P.; Mitchell, K.; Robinson, B.; Yu, E.; Ray, P. C. *Chem.—Eur. J.* **2009**, *15*, 342.
- (42) Tang, F.; He, F.; Cheng, H. C.; Li, L. D. *Langmuir* **2010**, *26*, 11774.
- (43) Kim, K.; Kim, H. S.; Park, H. K. *Langmuir* **2006**, *22*, 8083.
- (44) Shang, L.; Chen, H.; Deng, L.; Dong, S. *Biosens. Bioelectron.* **2008**, *23*, 1180.
- (45) Kim, K.; Lee, H. S. *J. Phys. Chem. B* **2005**, *109*, 18929.
- (46) Huang, G. G.; Han, X. X.; Hossain, M. K.; Ozaki, Y. *Anal. Chem.* **2009**, *81*, 5881.
- (47) Wu, H.; Tang, B.; Wu, P. *J. Phys. Chem. C* **2011**, *116*, 2246.
- (48) Zhao, Y.; Hao, C.; Ma, W.; Yong, Q.; Yan, W.; Kuang, H.; Wang, L.; Xu, C. *J. Phys. Chem. C* **2011**, *115*, 20134.
- (49) Wong, Y. J.; Zhu, L.; Teo, W. S.; Tan, Y. W.; Yang, Y.; Wang, C.; Chen, H. *J. Am. Chem. Soc.* **2011**, *133*, 11422.
- (50) Huang, J.; Kim, K. H.; Choi, N.; Chon, H.; Lee, S.; Choo, J. *Langmuir* **2011**, *27*, 10228.
- (51) Cui, Y.; Zheng, X.-S.; Ren, B.; Wang, R.; Zhang, J.; Xia, N. S.; Tian, Z.-Q. *Chem. Sci.* **2011**, *2*, 1463.
- (52) Dong, H.; Yan, F.; Ji, H.; Wong, D. K. Y.; Ju, H. *Adv. Funct. Mater.* **2010**, *20*, 1173.